# ESI

## Cu(111)@metal-organic framework as a tandem catalyst for highly Selective $CO_2$ electroreduction to $C_2H_4$

*Zhen-Hua Zhao, Kai Zheng, Ning-Yu, Huang, Hao-Lin Zhu, Jia-Run Huang, Pei-Qin Liao,* Xiao-Ming Chen*

*MOE Key Laboratory of Bioinorganic and Synthetic Chemistry, School of Chemistry, Sun Yat-Sen University, Guangzhou 510275, China.*

*E-mail: liaopq3@mail.sysu.edu.cn

## Materials and Methods:

### Chemical

All reagents involved in our study were commercially available and used without further purification. Tetrahydroxy-1,4-benzoquinone hydrate (THQ) was purchased from TCI (Shanghai), China. Copper nitrate hydrate ($Cu(NO_3)_2 \cdot H_2O$) was purchased from Aladdin (Shanghai), China.

### Characterization

Powder X-ray diffraction (PXRD) was carried out on a Bruker D8-Focus Bragg−Brentano X-ray powder diffractometer equipped with a Cu sealed tube (λ = 1.54178 Å) at 40 kV and 40 mA (Cu Kα). Scanning electron microscopy (SEM) analysis was performed on a field emission-scanning electron microscope (SU8010 system). Transmission electron microscope (TEM) images were recorded by a TEM Jem-2100F Jeol working at 200 kV. X-ray photoelectron spectroscopy (XPS) measurements were carried out on an ESCALAB 250 spectrometer. Nuclear magnetic resonance (NMR) measurement was performed on a Bruker advance III. Attenuated total reflection Fourier transform infrared spectroscopy (ATR-FTIR) experiments were performed on a Nicolet 6700 spectrometer.

### Synthesis of Cu-THQ

Tetrahydroxyquinone (THQ) (300 mg, 1.74 mmol) was dissolved in 100 mL degassed $H_2O$ under the $N_2$ protection. Mixture of $Cu(NO_3)_2 \cdot 2.5H_2O$ (532 mg, 2.29 mmol) and ethylenediamine (0.23 mL, 3.45 mmol) in 100 mL degassed $H_2O$ was transferred to THQ solution under vigorous stirring. The reaction was further stirred for at 500 rpm for 12 h at RT under the $N_2$. Dark navy precipitate was obtained and filtered. The product was subsequently washed with $H_2O$ (100 mL × 2) and acetone (50 mL × 2) and dried in 80 °C oven for further characterizations (Yield: 81.4%).

### Synthesis of Cu(111)@Cu-THQ

5 mg **Cu-THQ** and 50 μL 5 wt% Nafion were dispersed in 0.95 mL water-ethanol solution with a volume ratio of 3:1 and ultrasonicated for 1 h. Then 10 μL of the resulting ink was dropped onto the surface of glass carbon electrode (GCE) with a glassy carbon (GC) disk of 5 mm in diameter and dried at room temperature. Electrochemical reduction measurements were performed in a three-electrode cell using the Ag/AgCl electrode as the reference electrode and Pt foil as the counter electrode in 0.1 M $KHCO_3$. After treating at a certain potential (−1.6 V *vs*. RHE) for 30 minutes, **Cu(111)@Cu-THQ** was obtained, which was used directly for the $CO_2$ electroreduction reaction ($CO_2RR$) measurements and other characterizations.

**$CO_2$ electroreduction reaction ($CO_2$RR) measurements.**

All the electrochemical experiments were performed in a H-type cell with two-compartments separated by a Nafion-117 membrane. Each compartment contained 40 ml electrolyte (0.1 M $KHCO_3$). Electrochemical measurements were performed in a three-electrode cell using the Ag/AgCl electrode as the reference electrode and Pt foil as the counter electrode. Typically, 5 mg of catalyst and 50 μL 5 wt% Nafion were dispersed in 0.95 mL water-ethanol solution with a volume ratio of 3:1 and sonicated for 1 h. Then 10 μL of the resulting ink was dropped onto the surface of glass carbon electrode (GCE) with a glassy carbon (GC) disk of 5 mm in diameter and dried at room temperature. During the electrochemical measurements, the electrolyte solution was purged with $CO_2$ for 30 min to obtain the $CO_2$-saturated solution (pH = 6.8). A mass flow controller was used to set the $CO_2$ flow rate at 20 mL/min. The LSV curves were conducted with scan rate of 10 mV/s. All the potentials were reported with respect to the reversible hydrogen electrode (RHE) without internal resistance (IR) compensation and conversed using the formula E (*vs*. RHE) = E (*vs*. Ag/AgCl) + 0.196 V + 0.059 × pH. The electrode was applied for constant voltage, the gas products were analyzed by the gas chromatograph linking to the cathode cell, which was equipped with two flame ionization detectors (FID) and thermal conductivity detector (TCD). Gaseous products generated during the electrocatalysis were detected by a 7890B system. The liquid products were analyzed afterwards by a 400 MHz NMR spectrometer using dimethyl sulphoxide (DMSO) as an internal standard. The Faraday efficiency of a certain gas product was calculated by the equation:

$$FE = \frac{PV}{T} \times \frac{\nu NF}{I}$$

in which $P$, $V$ and $T$ represent the pressure (1 atm), gas flow rate (20 mL $min^{-1}$) and room temperature, and $\nu$ (vol %), $I$, $N$, and $F$ represent the volume concentration of gas product, current, number of the electron transfer in electrocatalysis, and Faradaic constant, respectively.

**Preparation of commercial Cu(111) electrode**

Typically, 5 mg fresh Cu-THQ and 50 μL 5 wt% Nafion were dispersed in 0.95 mL water-ethanol solution with a volume ratio of 3:1 and sonicated for 1 h. Then 10 μL of the resulting ink was dropped onto the surface of glass carbon electrode (GCE) with a glassy carbon (GC) disk of 5 mm in diameter and dried at room temperature. After treating at a certain potential (−1.6 V *vs*. RHE) for 10.5 h, Cu(111) was obtained.

**Computational methods:**

Density functional theory (DFT) calculations were performed by the Materials Studio 5.5 package. The structures of intermediates were optimized by Dmol$^3$ module (Figure S14). The

generalized gradient approximation (GGA) with the Perdew- Burke-Ernzerhof (PBE) function and TS for DFT-D correction were employed to the calculation. The convergence tolerance of energy, force and displacement convergence were set as $1 \times 10^{-5}$ Ha, $2 \times 10^{-3}$ Ha and $5 \times 10^{-3}$ Å, respectively. The core treatment was chosen as the effective core potential (ECP), and the electron treatment was performed by double numerical plus d-functions (DNP) basis set.

The elementary steps on MOFs are:

$* + CO_2 + [H^+ + e^-] \rightarrow *COOH$

$*COOH + [H^+ + e^-] \rightarrow *CO + H_2O$

$*CO \rightarrow * + CO$

The elementary steps on Cu(111) are:

$* + CO \rightarrow *CO$

$*CO + CO + [H^+ + e^-] \rightarrow *COCHO$

$*COCHO + [H^+ + e^-] \rightarrow *COCHOH$

$*COCHOH + [H^+ + e^-] \rightarrow *COHCHOH$

$*COHCHOH + 2[H^+ + e^-] \rightarrow *CHCHOH + H_2O$

$*CHCHOH + 2[H^+ + e^-] \rightarrow *CHCH_2 + H_2O$

$* CHCH_2 + [H^+ + e^-] \rightarrow * + C_2H_4$

The change of free energies for every step were calculated by the following reaction equation:

$$\Delta G = \Delta E + \Delta ZPE - T\Delta S$$

in which ΔZPE, Δ$T$ and Δ$S$ represent the change of the zero point energy, temperature (298.15 K), and the change of entropy, respectively.

## Supplementary Figures and Tables

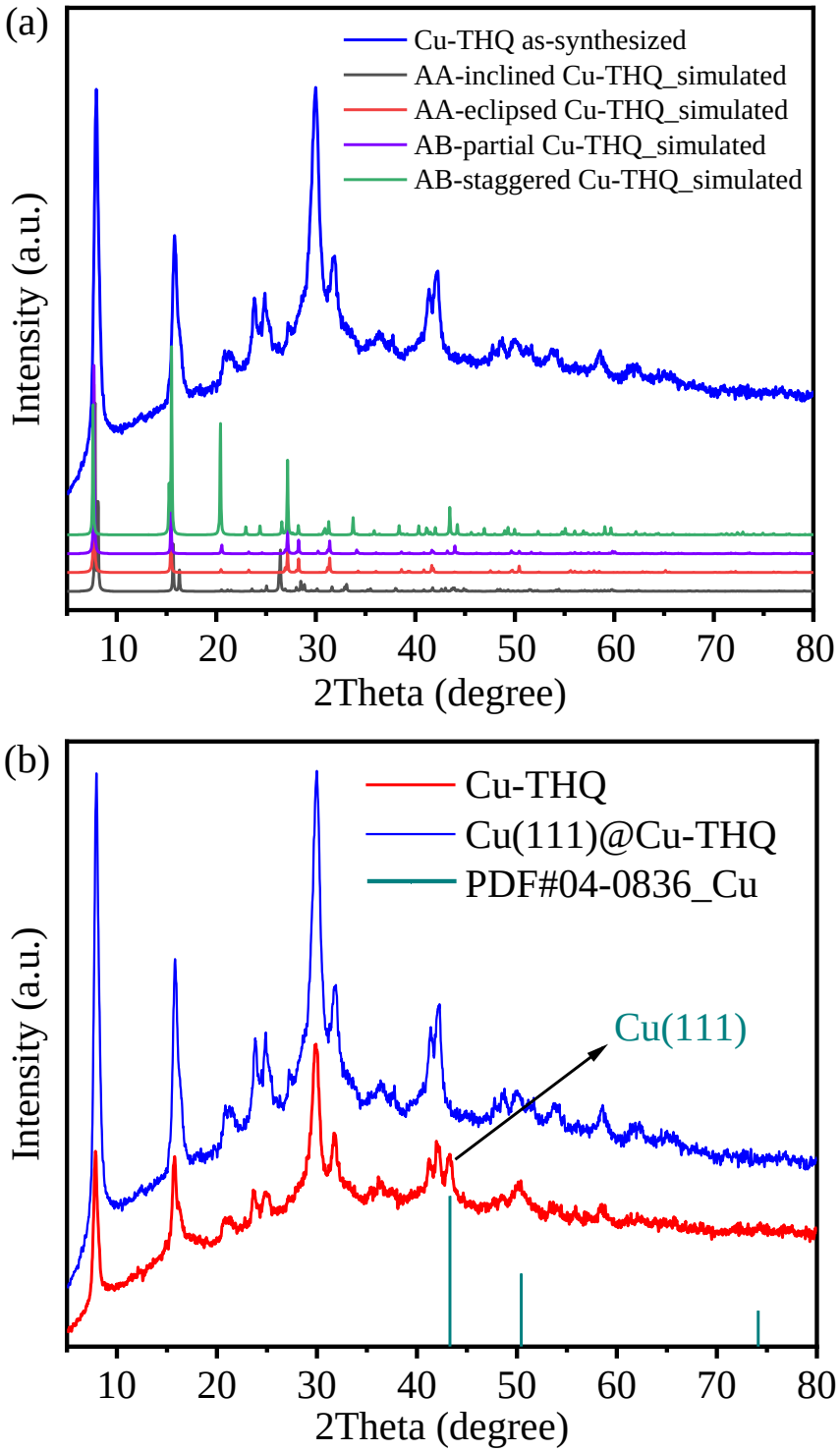


**Fig. S1.** PXRD patterns of the corresponding materials: **(a) Cu-THQ** and **(b) Cu(111)@Cu-THQ.** Note: The **Cu-THQ** sample has a diffraction peak at 50.4°, which is similar to the peak position of the Cu(200) facet. However, no Cu nanoparticles were

found in the transmission electron microscopy of **Cu-THQ**, indicating that the diffraction peak at 50.4° belongs to **Cu-THQ** itself (same as the simulated pattern). Comparison of the PXRD spectra of Cu-THQ and Cu(111)@Cu-THQ shows clearly that **Cu(111)@Cu-THQ** has a new diffraction peak at 43.3°, which is attributed to the Cu(111) facet. In addition, the peak intensity of **Cu(111)@Cu-THQ** at 50.4° (200) and 74.1° (220) did not increase significantly, proving that there are no Cu(200) and Cu(220) facets.

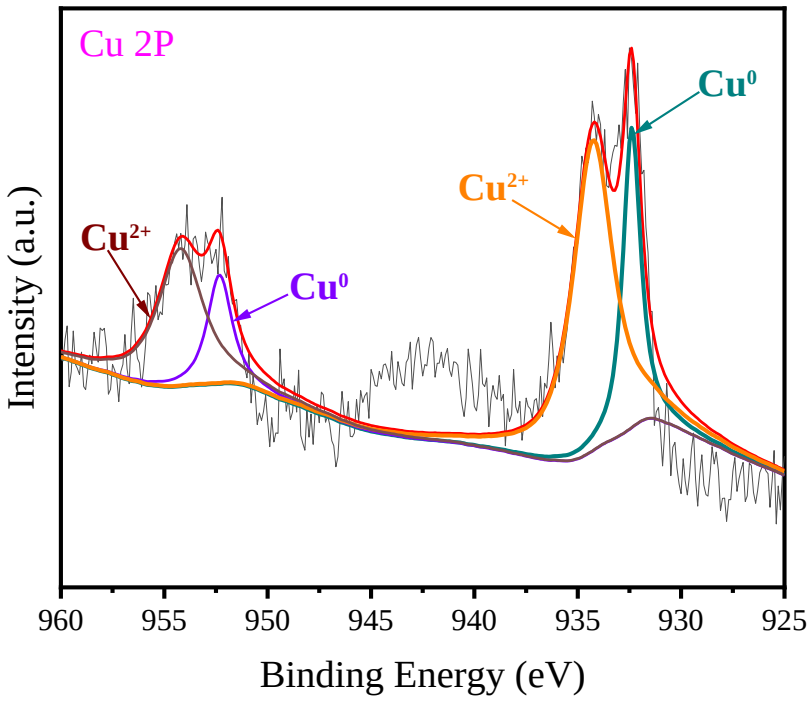


**Fig. S2.** X-ray photoelectron spectroscopy (XPS) spectra of **Cu(111)@Cu-THQ**.

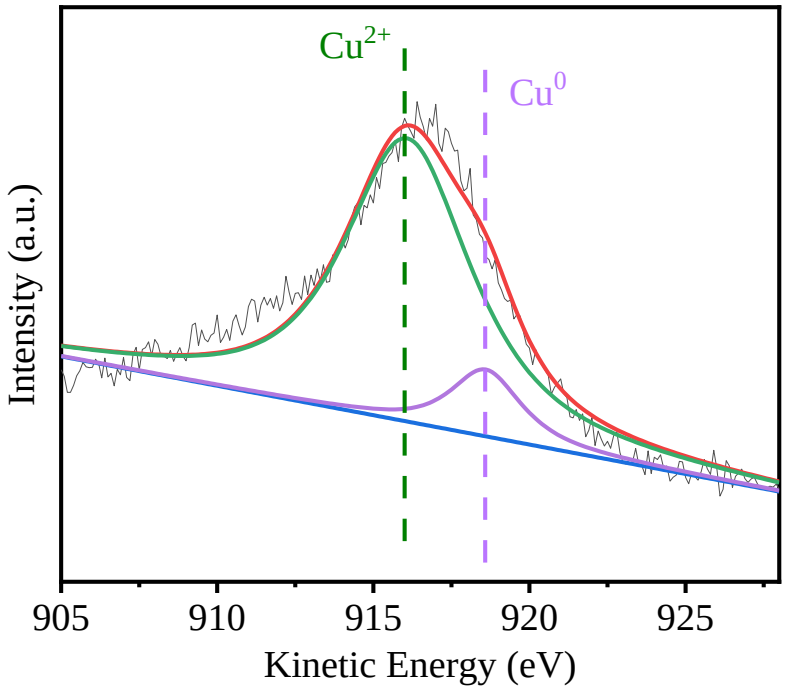


**Fig. S3.** Cu LMM spectra of as-prepared **Cu(111)@Cu-THQ**.

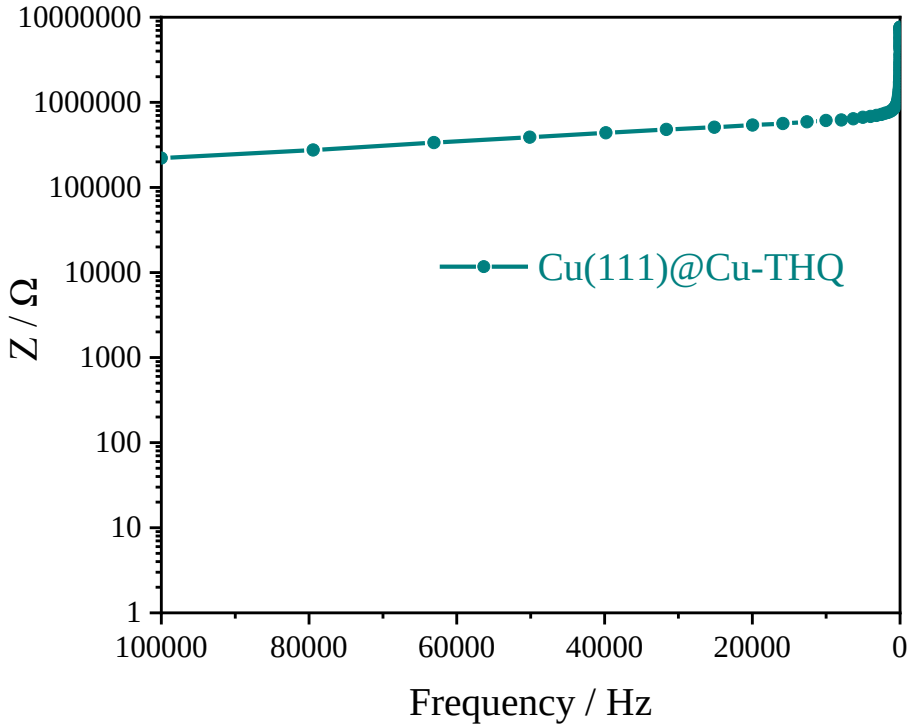


**Fig. S4.** Bode plot of electrochemical impedance spectroscopy of **Cu(111)@Cu-THQ.**

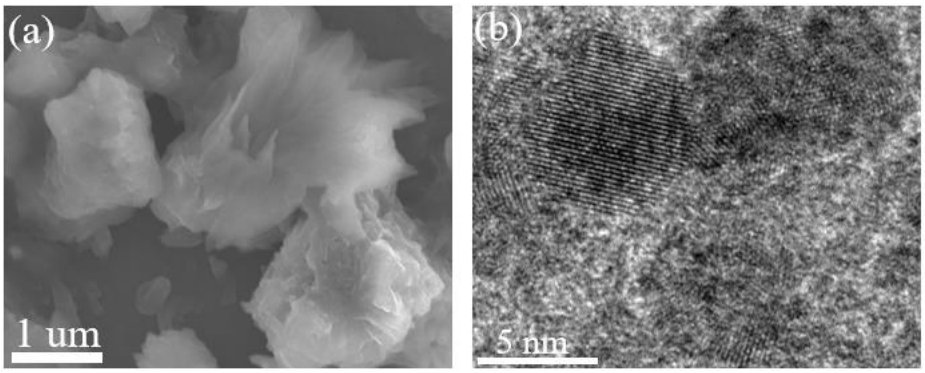


**Fig. S5**. **(a)** SEM and **(b)** TEM images of **Cu(111)@Cu-THQ** after electroreduction treatment at −1.4 V *vs.* RHE for 8.5 h.

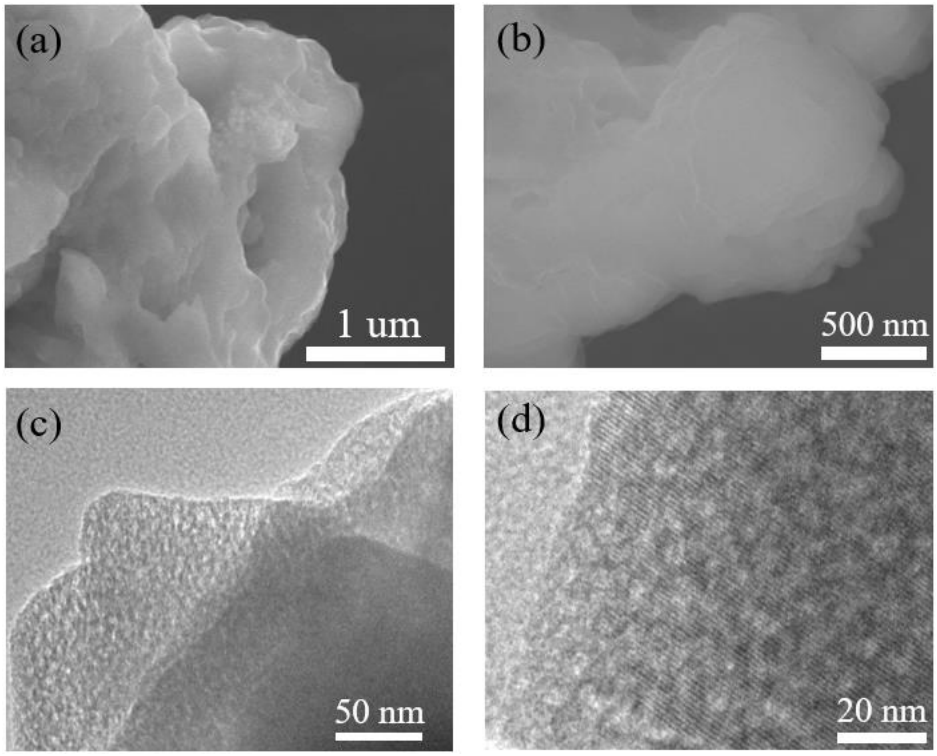


**Fig. S6**. **(a-b)** SEM and **(c-d)** TEM images of the fresh **Cu-THQ**.

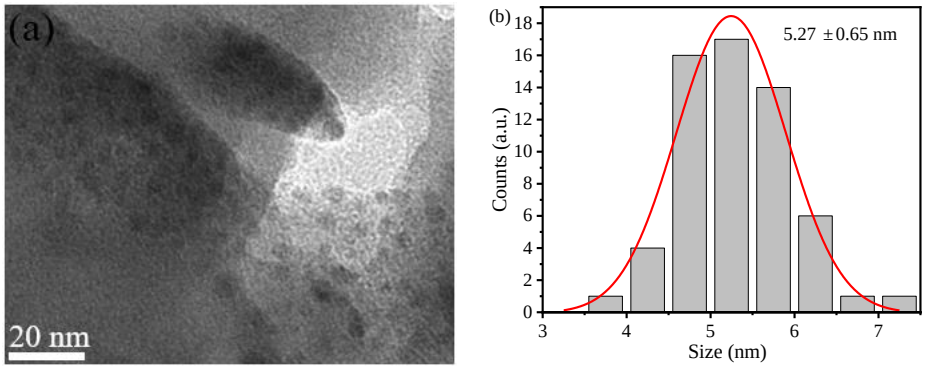


**Fig. S7. (a)** The TEM image of **Cu(111)@Cu-THQ** after electroreduction treatment at −1.4 V *vs.* RHE for 2.5 h and **(b)** the corresponding particle size distribution graph.

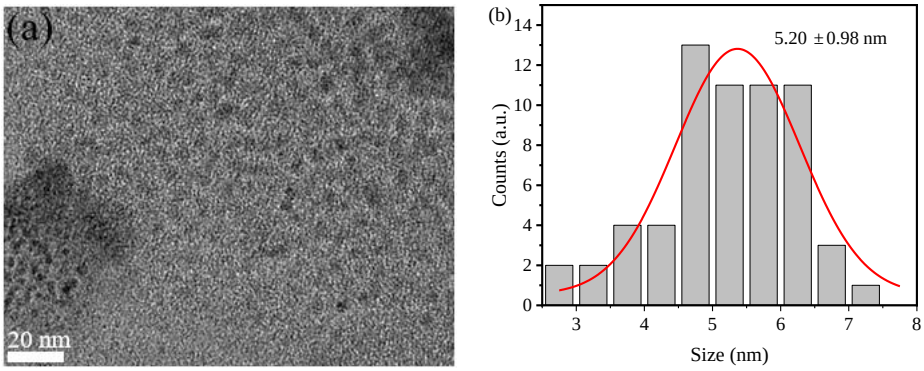


**Fig. S8. (a)** The TEM image of **Cu(111)@Cu-THQ** after electroreduction treatment at −1.4 V *vs.* RHE for 4.5 h and **(b)** the corresponding particle size distribution graph.

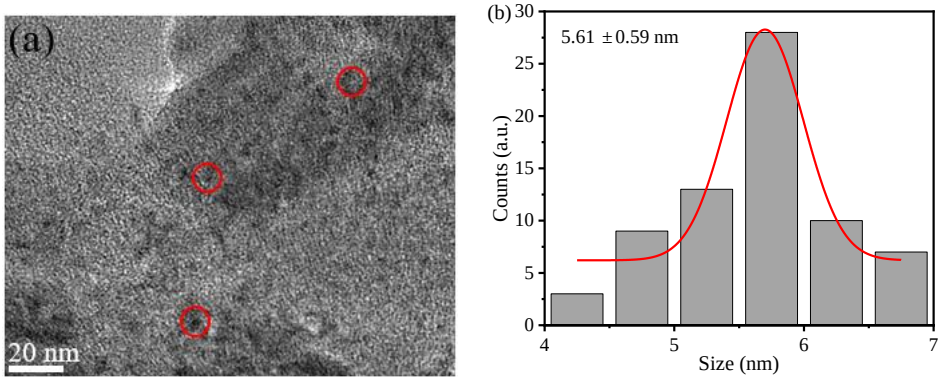


**Fig. S9. (a)** The TEM image of **Cu(111)@Cu-THQ** after electroreduction treatment at −1.4 V *vs.* RHE for 8.5 h and **(b)** the corresponding particle size distribution graph.

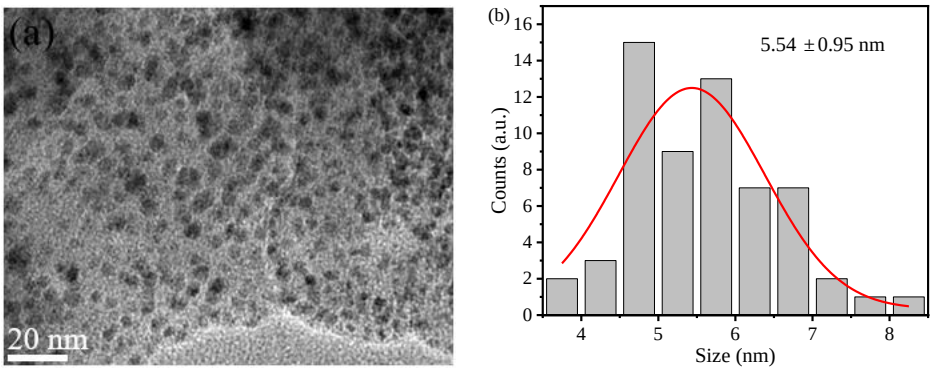


**Fig. S10. (a)** The TEM image of **Cu(111)@Cu-THQ** obtained by electroreduction treatment of **Cu-THQ** at −1.6 V *vs.* RHE for 30 minutes and **(b)** the corresponding particle size distribution graph.

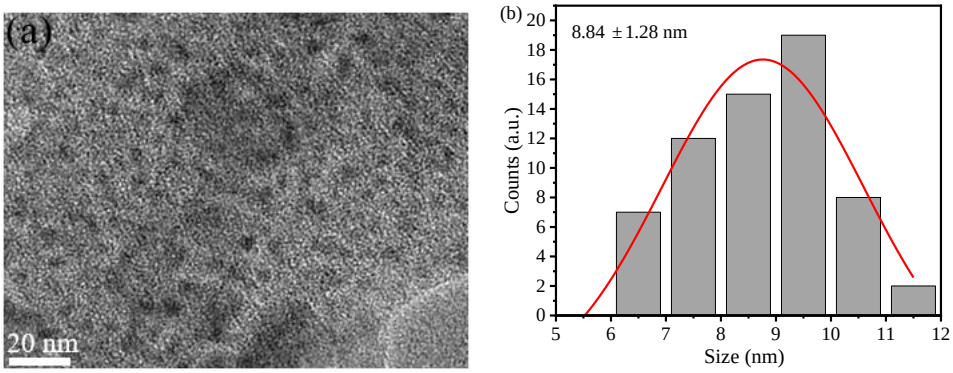


**Fig. S11. (a)** The TEM image of **Cu(111)@Cu-THQ** after electroreduction treatment at −1.6 V *vs.* RHE for 4.5 h and **(b)** the corresponding particle size distribution graph.

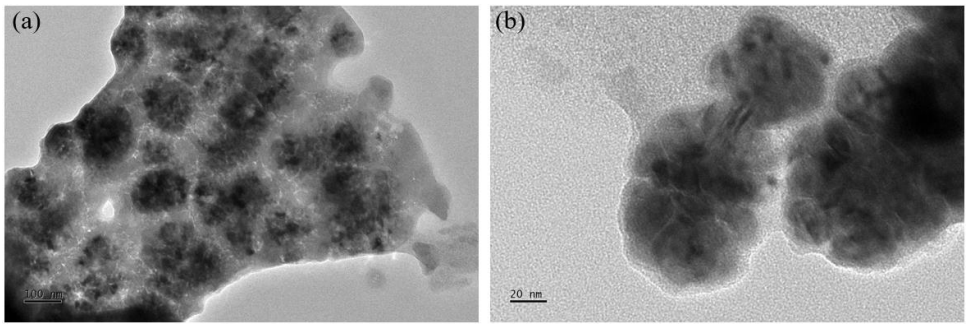


**Fig. S12. (a)** and **(b)** The TEM images of **Cu(111)@Cu-THQ** after electroreduction treatment at −1.6 V *vs.* RHE for 8.5 h.

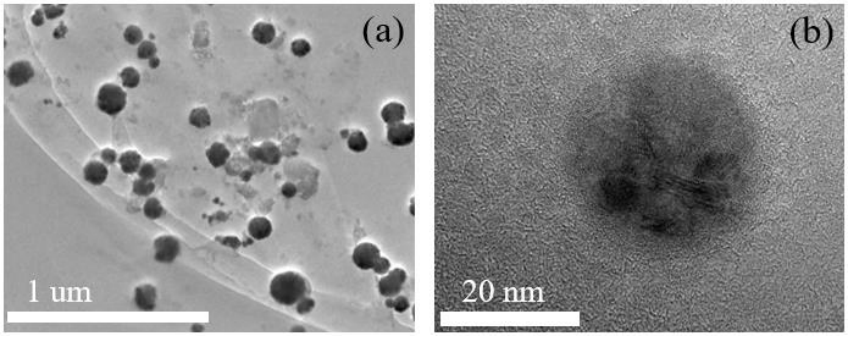


**Fig. S13**. **(a)** and **(b)** TEM images of the pure Cu(111) nanoparticles.

At −1.4 V *vs.* RHE, the particle sizes of the Cu nanoparticles of **Cu(111)@Cu-THQ** after working ($CO_2$RR process) for 2.5, 4.5 and 8.5 h were similar, about 5±1 nm.

At −1.6 V *vs.* RHE, the particles sizes of the Cu nanoparticles increased from 5 to 10 nm with the increase of the reduction time from 30 min to 8.5 hours. After 10.5 hours' reduction, most of the MOF structure was destroyed.

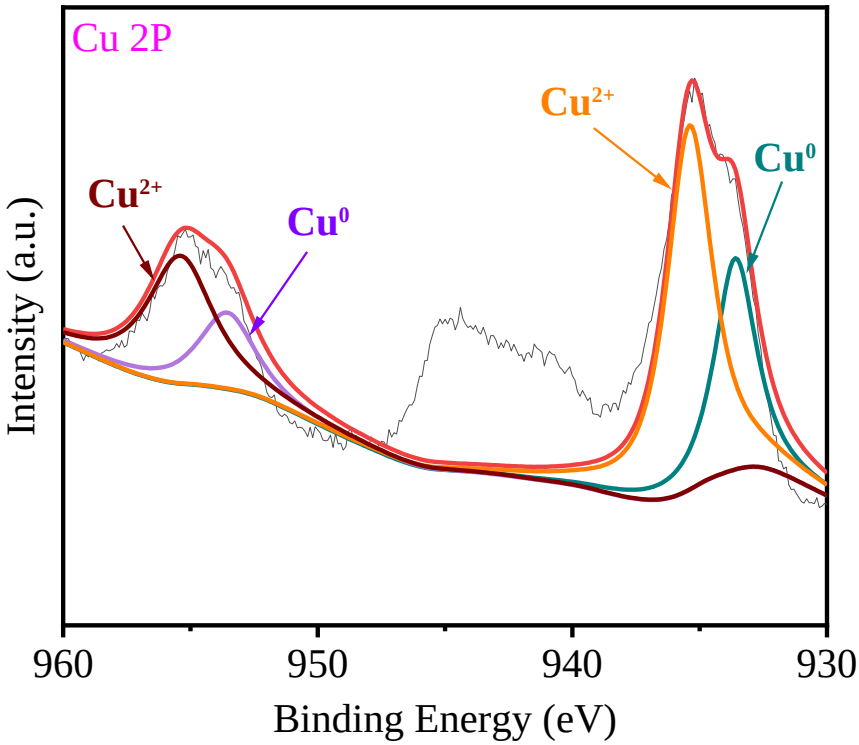


**Fig. S14.** The X-ray photoelectron spectroscopy (XPS) spectra of **Cu(111)@Cu-THQ** obtained by electroreduction treatment at −1.4 V *vs.* RHE for 2.5 h.

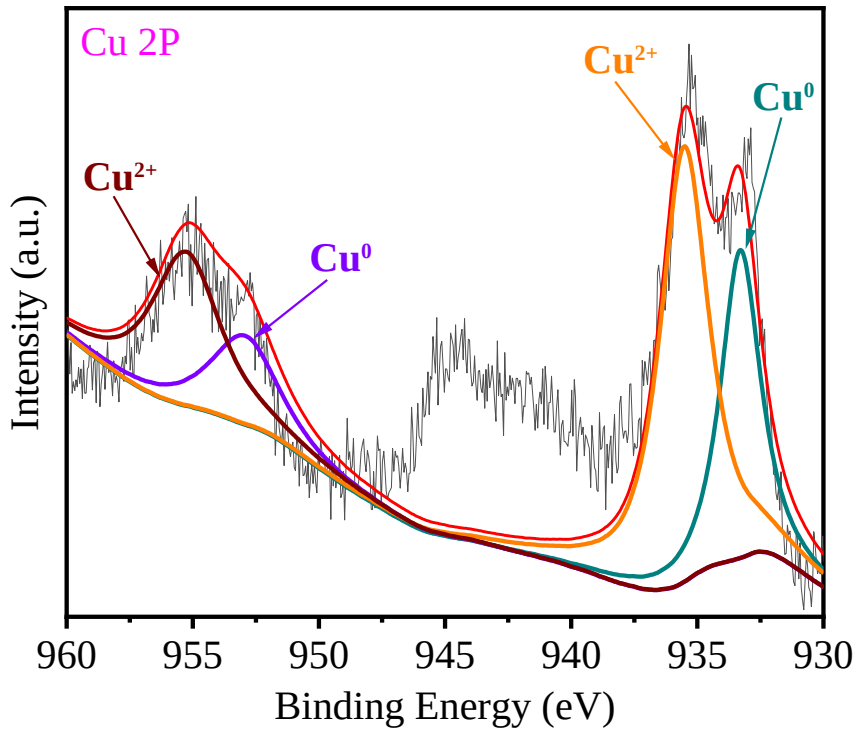


**Fig. S15.** The X-ray photoelectron spectroscopy (XPS) spectra of **Cu(111)@Cu-THQ** obtained by electroreduction treatment at −1.4 V *vs.* RHE for 4.5 h.

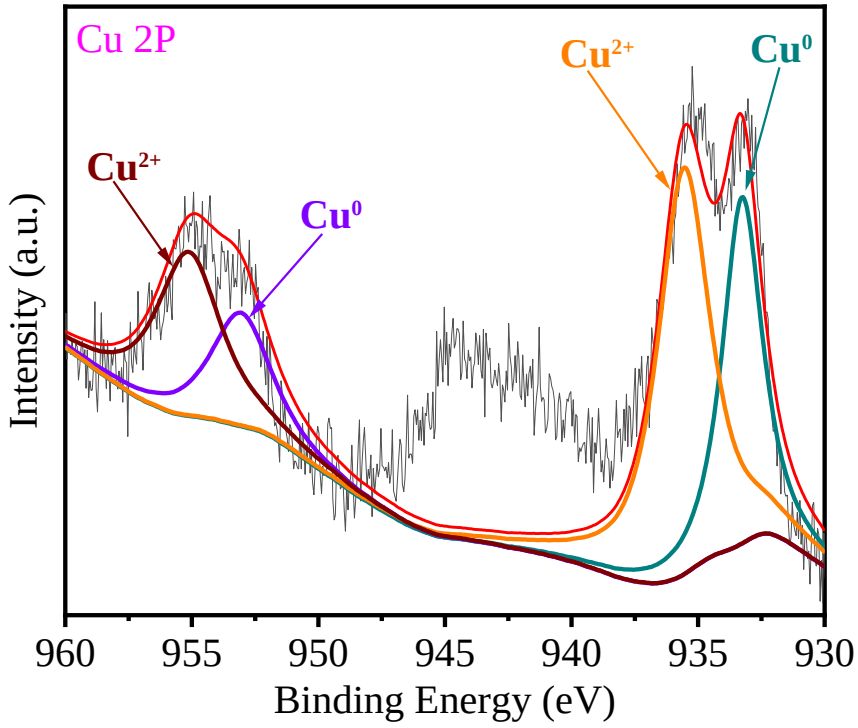


**Fig. S16.** The X-ray photoelectron spectroscopy (XPS) spectra of **Cu(111)@Cu-THQ** obtained by electroreduction treatment at −1.4 V *vs.* RHE for 8.5 h.

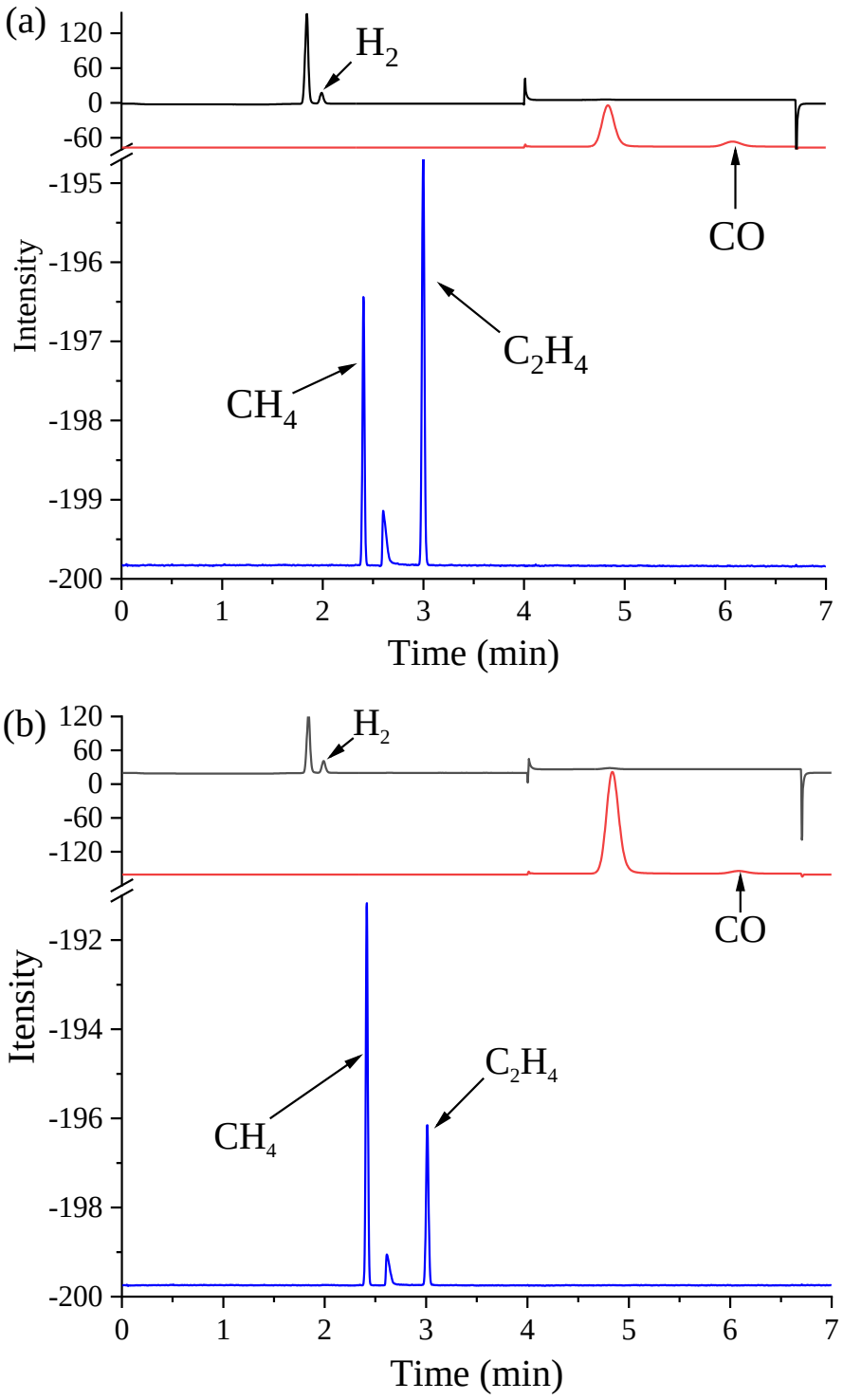


**Fig. S17.** GC profiles of gas products of **Cu(111)@Cu-THQ** at −1.4 V *vs*. RHE **(a)** and −1.6 V *vs*. RHE **(b)**.

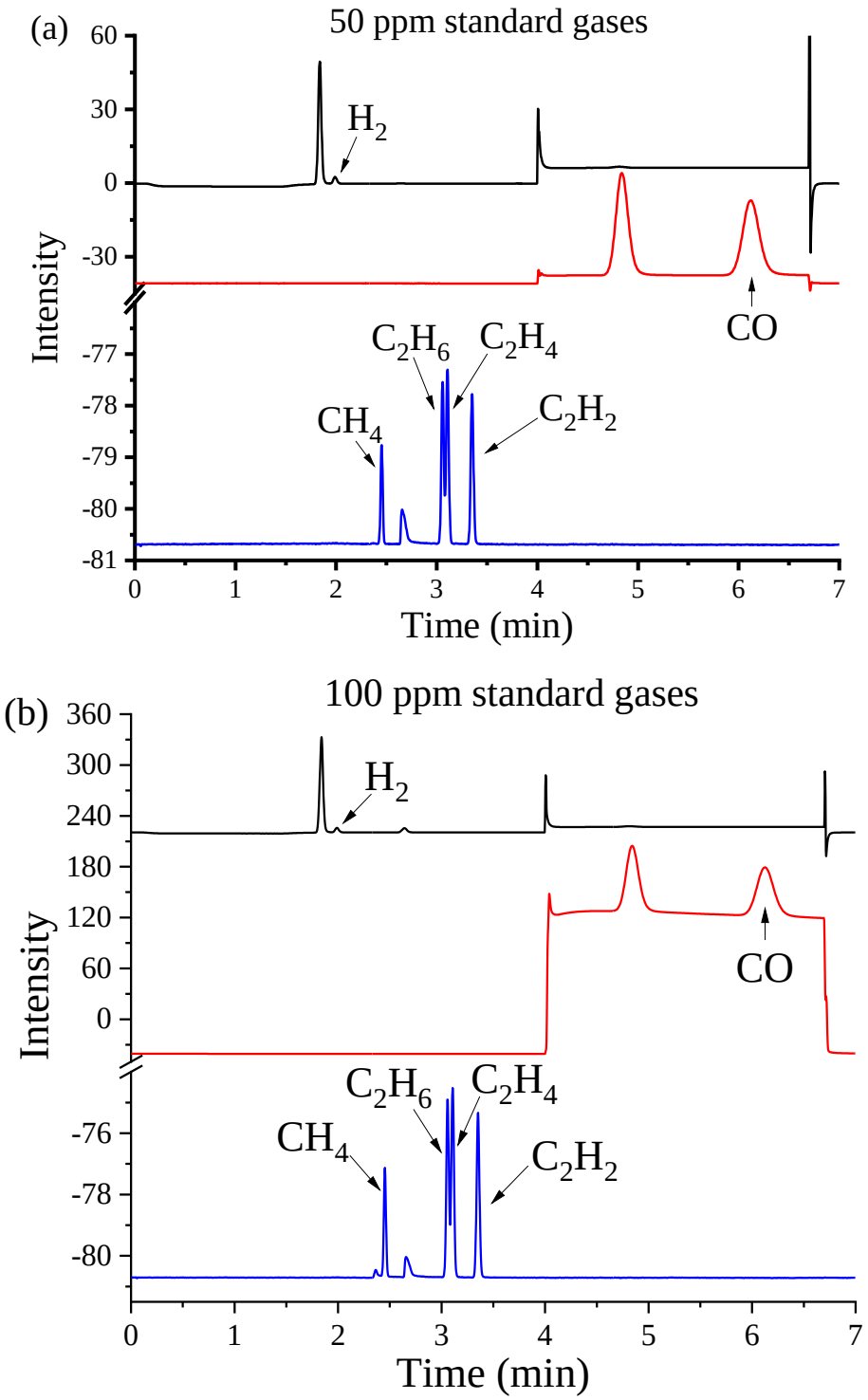


**Fig. S18.** The GC profiles of the standard gas of different concentrations: **(a)** 50 ppm and **(b)** 100 ppm.

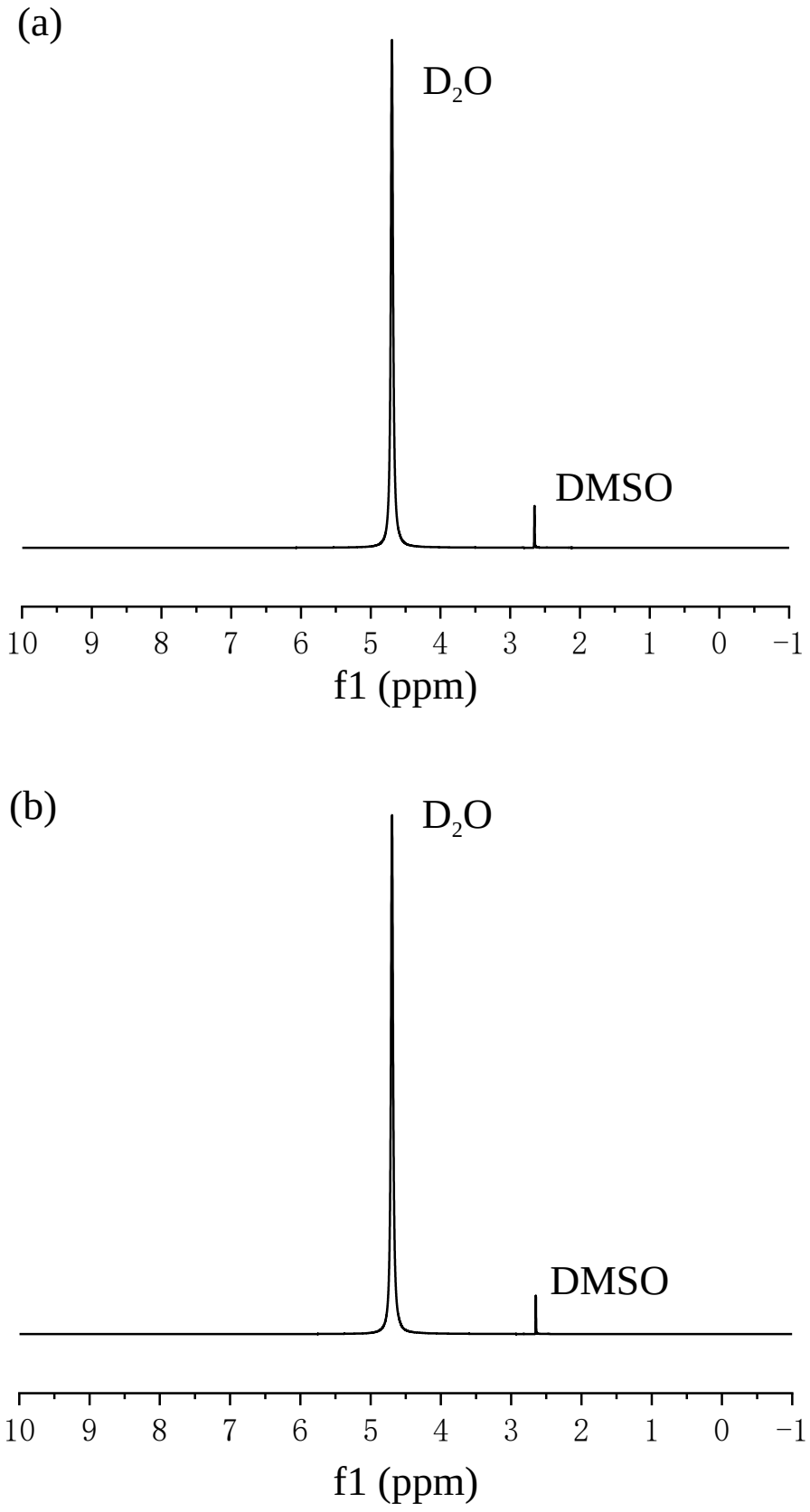


**Fig. S19.** The $^{1}$H nuclear magnetic resonance ($^{1}$H NMR) spectra of the liquid phase. **(a)** fresh electrolyte (0.1 M $KHCO_3$); **(b)** after electrocatalysis electrolyte.

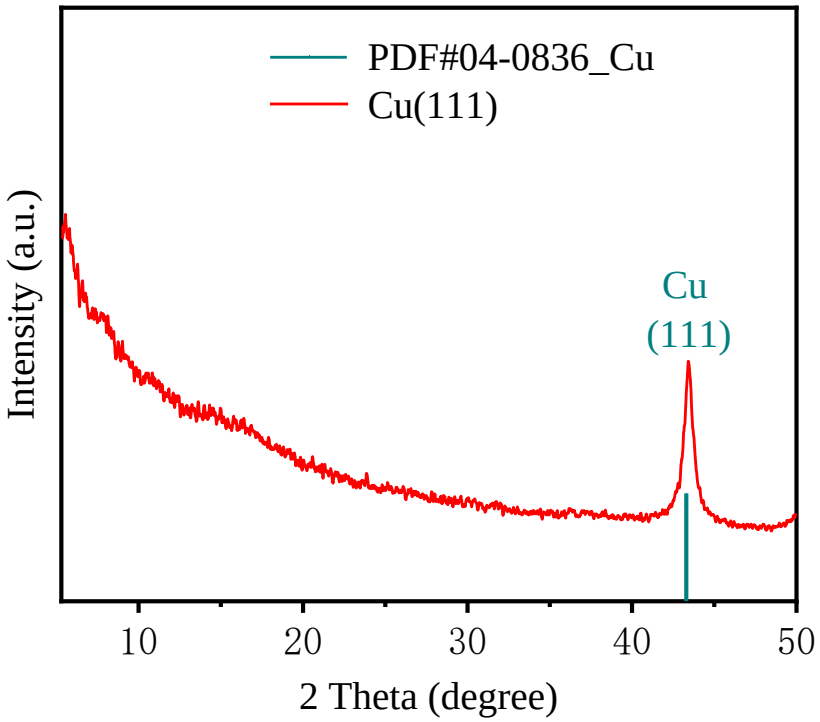


**Fig. S20.** PXRD pattern of Cu(111)**.**

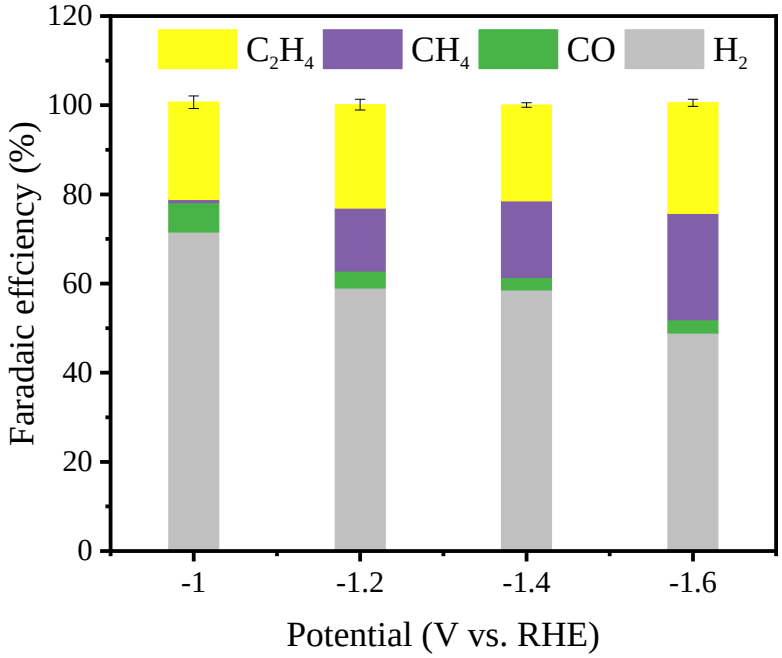


**Fig. S21.** Faradaic efficiencies of different products for Cu(111).

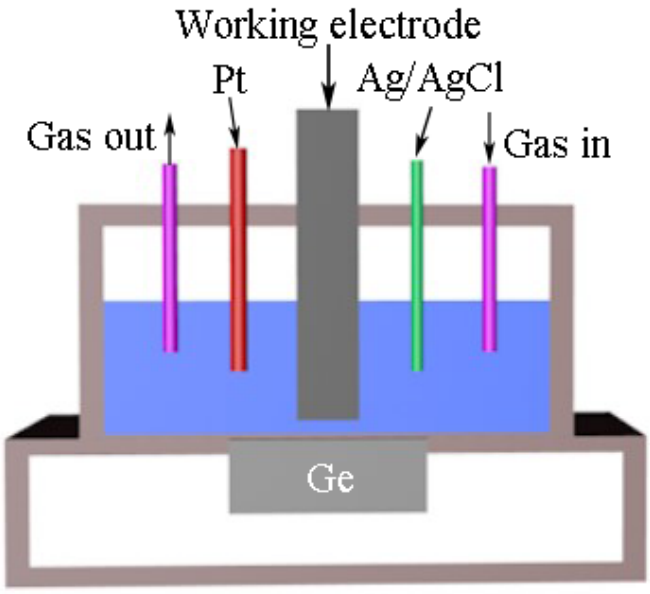


**Fig. S22.** Illustration of the ATR-FTIR system used for *in-situ* characterization.

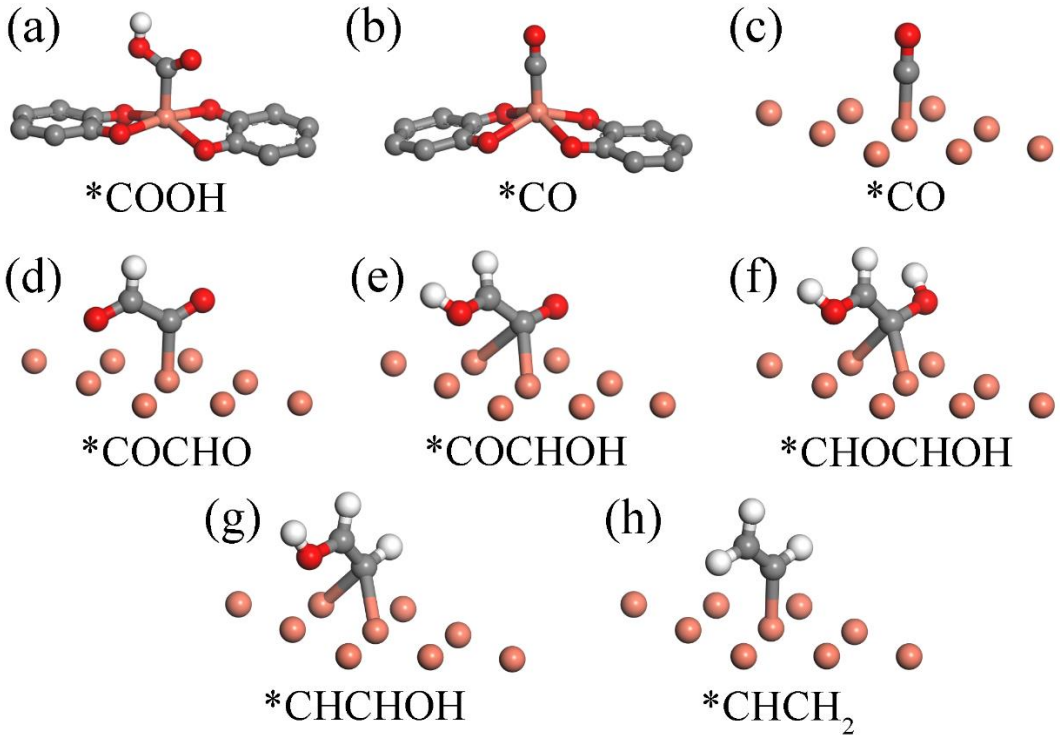


**Fig. S23.** The DFT-simulated intermediate structures. (a) and (b) are the corresponding intermediates on the MOF, the latter are the corresponding intermediates on the Cu(111) (color codes: orange is Cu, gray is C, red is O, white is H).

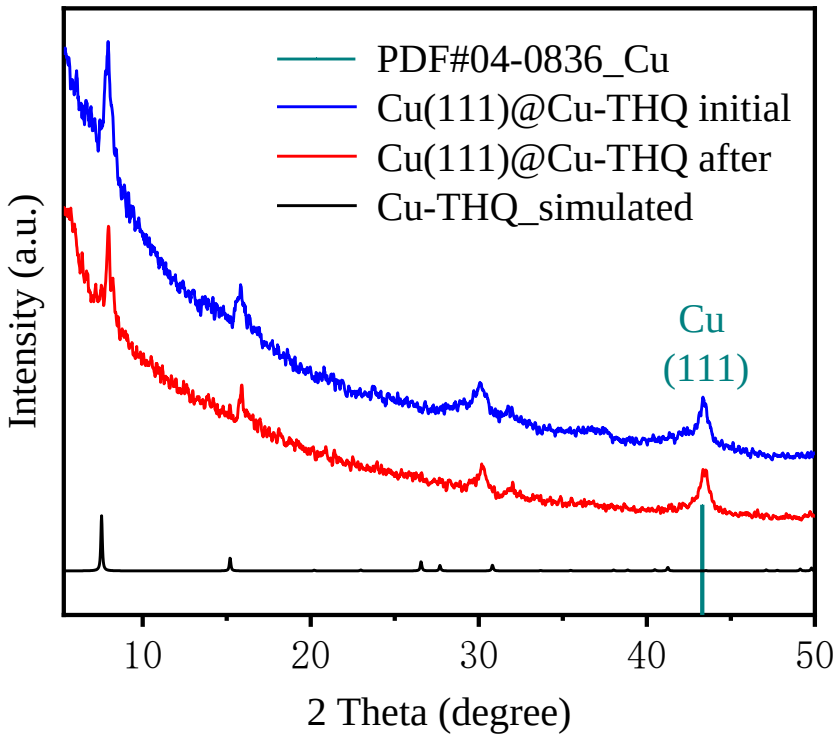


**Fig. S24.** PXRD patterns of **Cu(111)@Cu-THQ** before and after electroreduction at −1.4 V *vs*. RHE for 8.5 hours.

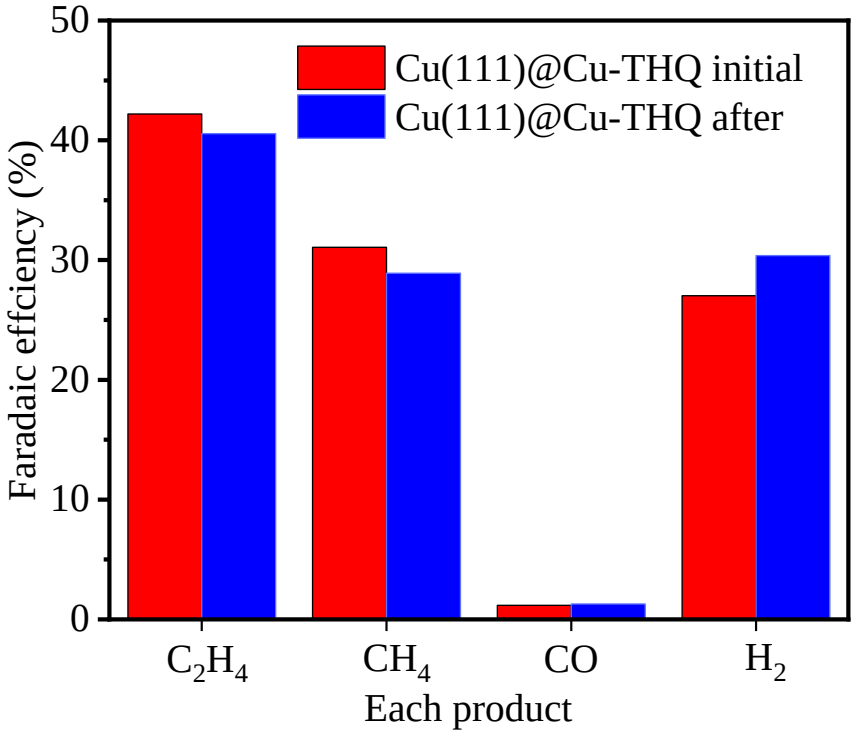


**Fig. S25.** The $CO_2RR$ performances of **Cu(111)@Cu-THQ** before and after electroreduction at −1.4 V *vs*. RHE for 8.5 hours.

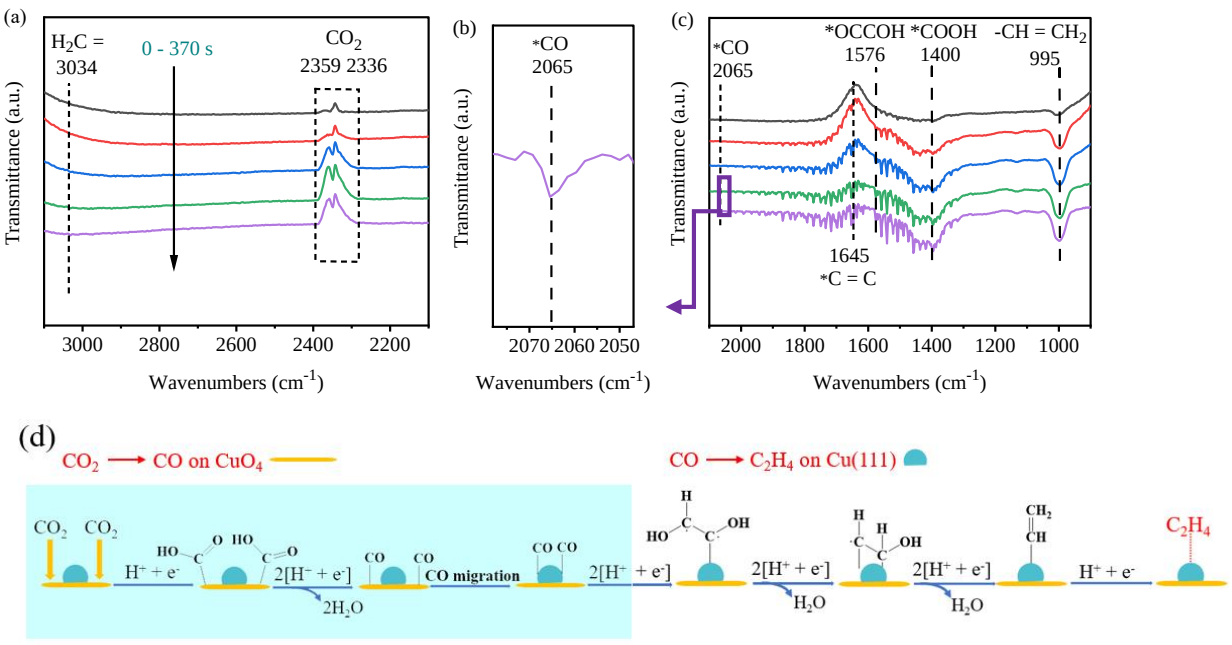


**Fig. S26.** (a-c) In-situ operando ATR-FTIR spectra on **Cu(111)@Cu-THQ** collected at -1.4 V *vs.* RHE in $CO_2$ saturated 0.1 M $KHCO_3$ electrolyte. (d) Proposed tandem catalytic mechanism of **Cu(111)@Cu-THQ** for the formation of $C_2H_4$.

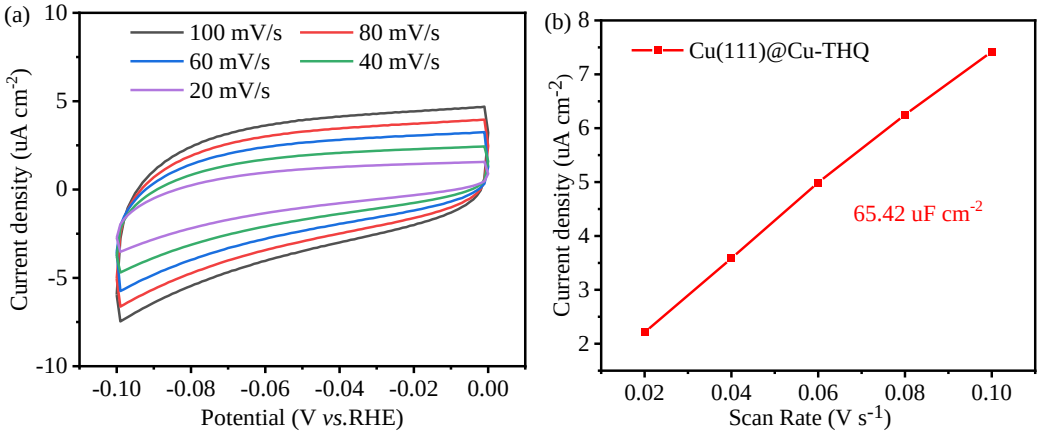


**Figure S27**. (a) Capacitive behaviors of **Cu(111)@Cu-THQ** and (b) plot of the current densities with different scan rates in the range 20 mV/s to 100 mV/s.

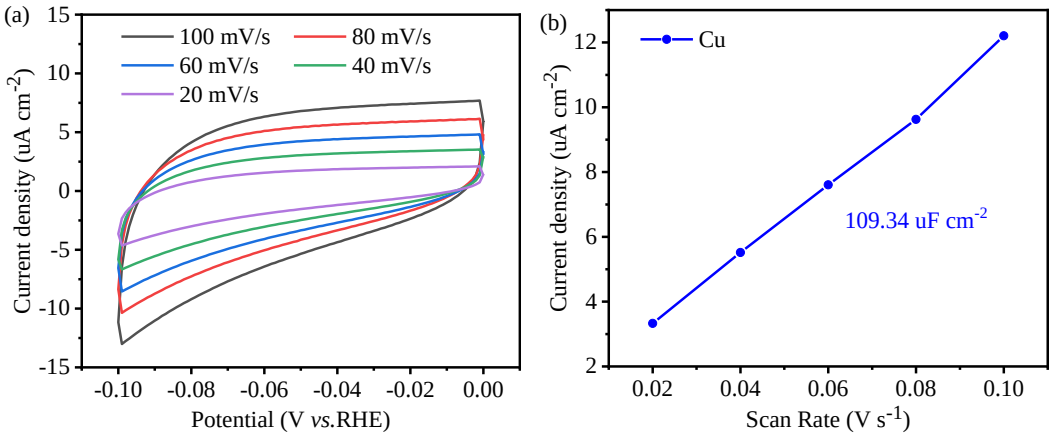


**Figure S28**. (a) Capacitive behaviors of Cu(111) and (b) plot of the current densities with different scan rates in the range 20 mV/s to 100 mV/s.

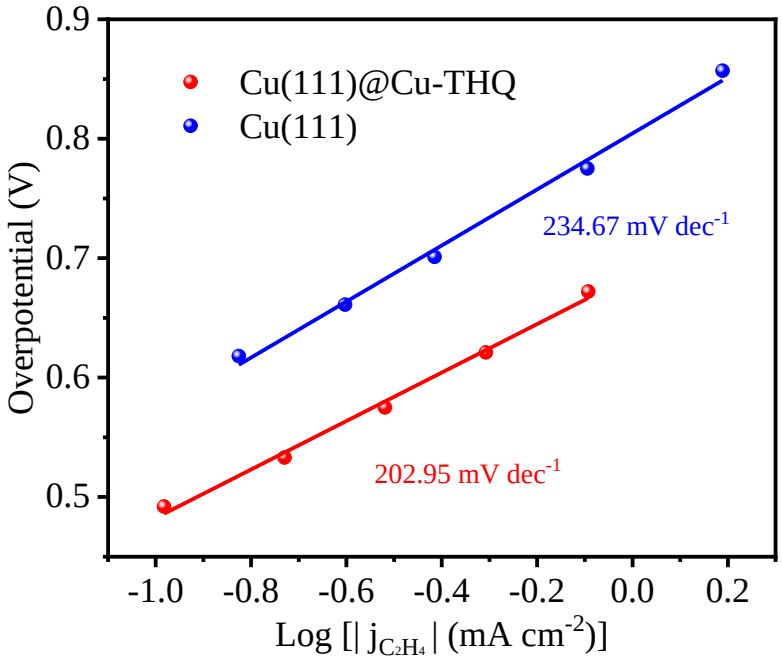


**Figure S29**. Tafel plots of **Cu(111)@Cu-THQ** and Cu(111).

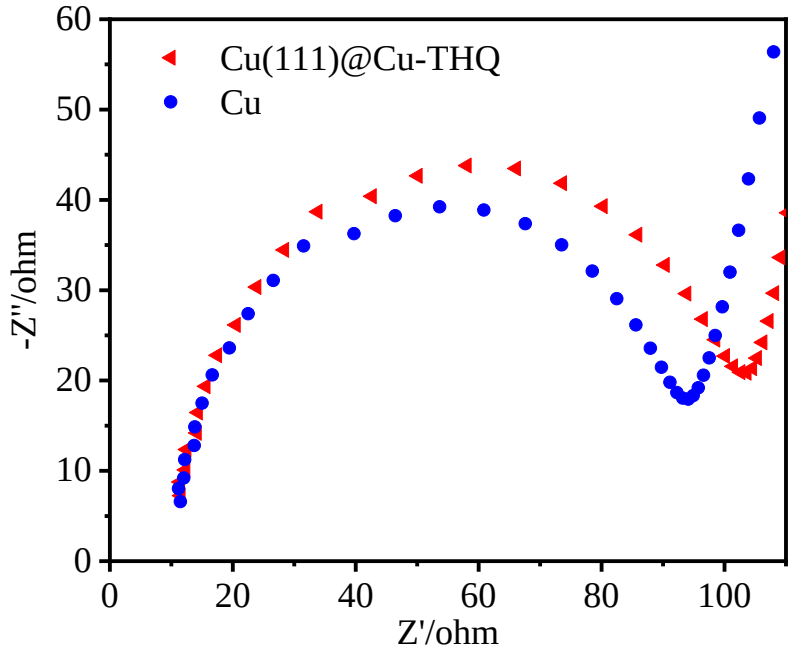


**Figure S30.** The Nyquist plots of the electrochemical impedance spectroscopy (EIS) measurement results of the electrocatalysts over the frequency ranging from 1000 kHz to 0.01 Hz at −0.053 V *vs.* RHE. Note: Due to the resistance of the electrolyte itself and the resistance between the electrolyte and the electrode, the starting point of Nyquist plots is not 0. Compared with Cu(111), the impedance of **Cu(111)@Cu-THQ** is slightly larger due to the presence of MOF.

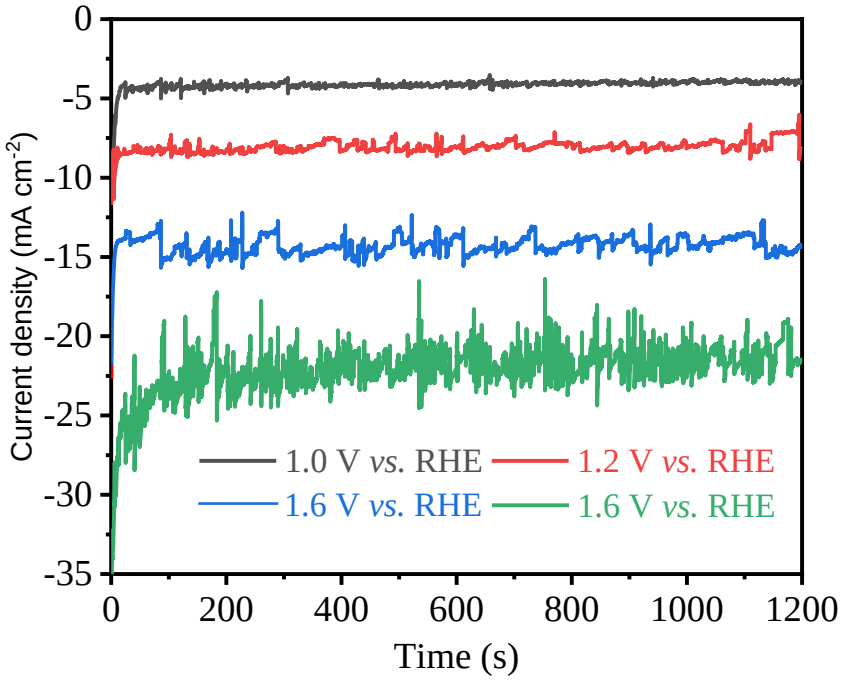


**Figure S31**. IT curves of **u(111)@Cu-THQ** for $CO_2$ reduction.

**Supplementary Table S1.** The $C_2H_4$ selectivity of $CO_2RR$ with various electrocatalysts using Pt as counter electrode under neutral conditions in the H-cell reported in the literature.

| Catalyst | Electrolyte | Potential (V) | Main product (FE/%) | Partial current density for $C_2H_4$ (mA cm$^{-2}$) | Stability / h | Ref. |
|---|---|---|---|---|---|---|
| Densely packed Cu particle | 0.1 M $KHCO_3$ solution | -0.86 (*vs.* RHE) | $C_2H_4$ (~34) $C_2H_5OH$ (~15) $CH_4$ (~5) | -- | 10 | [30] |
| Cu mesocrystals | 0.1 M $KHCO_3$ solution | -0.99 (*vs.* RHE) | $C_2H_4$ (27.2) $CH_4$ (1.47) | -- | ~6 | [31] |
| 44 nm Cu nanocube | 0.1 M $KHCO_3$ solution | -1.1 (*vs.* RHE) | $C_2H_4$ (~40) $CH_4$ (~20) | -- | 1 | [32] |
| CuO/$N_x$ C-700 °C | 0.1 M $NaHCO_3$ solution | -1.25 (*vs.* RHE) | $C_2H_4$ (36) $CH_4$ (~14 | -- | ~1 | [33] |
| Cu nanocube-O | 0.1 M $KHCO_3$ solution | -1.0 (*vs.* RHE) | $C_2H_4$ (45) $C_2H_5OH$ (~22.5) | ~15 | 0.25-0.3 | [34] |
| KF cycled Cu foil | 0.1 M $KHCO_3$ solution | -1.0 (*vs.* RHE) | $C_2H_4$ (16.3) $C_2H_5OH$ (7.9) | -- | -- | [35] |
| 8.1 μm Cu nanowire | 0.1 M $KHCO_3$ solution | -1.1 (*vs.* RHE) | $C_2H_4$ (17.4) $C_2H_5OH$ (~5) $C_2H_6$ (2) CO (~10) n-propanol (~10) | -- | 5 | [36] |
| Polycrystalline Cu with N-tolylpyridinium chloride | 0.1 M $KHCO_3$ solution | -1.1 (*vs.* RHE) | $C_2H_4$ (~40) | ~0.13 | 10 | [37] |
| $Cu_4Zn$ | 0.1 M $KHCO_3$ solution | -1.05 (*vs.* RHE) | $C_2H_4$ (~10) $C_2H_5OH$ (~30) CO (~10) | -- | 10 | [38] |
| Single-atomic Cu-substituted $CeO_2$ | 0.1 M $KHCO_3$ solution | -1.8 (*vs.* RHE) | $C_2H_4$ (~15) $CH_4$ (58) | 70 | 2.2 | [39] |
| Cu/$MoS_2$ | 0.1 M $NaHCO_3$ solution | -1.4 (*vs.* Ag/AgCl) | $C_2H_4$ (2.93) $CH_4$ (17.08) | ~4 | 48 | [40] |
| Polycrystalline Cu | 0.1 M $NaHCO_3$ solution | -1.6 (*vs.* Ag/AgCl) | $CH_4$ (50) $C_2H_4$ (10) | ~4 | 1 | [41] |

| | | | | | | |
|---|---|---|---|---|---|---|
| Cu nanoparticle | 0.1 M $KHCO_3$ solution | -1.1 (*vs.* RHE) | $CH_4$ (~20) $C_2H_4$ (~15) | ~1.1 | -- | [42] |
| Cu foil | 0.1 M $KHCO_3$ solution | -1.1 (*vs.* RHE) | $CH_4$ (57) $C_2H_4$ (~20) | 23 | -- | [23a] |
| Polished Cu foil | 0.3 M KI + 0.1 M $KHCO_3$ solution | -1.0 (*vs.* RHE) | $CH_4$ (~56) $C_2H_4$ (~23) | -- | 0.17 | [43] |
| $Cu_2O$ film | 0.1 M $KHCO_3$ solution | -0.99 (*vs.* Ag/AgCl) | $CH_4$ (9.85) $C_2H_4$ (32.92) | 1 | -- | [44] |
| $CuO_x$ nanoparticle | 0.1 M $KHCO_3$ solution | -1.0 (*vs.* RHE) | $CH_4$ (~19) $C_2H_4$ (~21) | ~1.3 | 6.7 | [45] |
| $Cu_2O$@HKUST-1 | 0.1 M $KHCO_3$ solution | -1.71 (*vs.* RHE) | $CH_4$ (63.2) $C_2H_4$ (16.2) | 8.4 | 1 | [46] |
| copper(II)-5,10,15,20-tetrakis(2,6-dihydroxyphenyl)porphyrin | 0.5 M $KHCO_3$ solution | -0.976 (*vs.* RHE) | $CH_4$ (~27) $C_2H_4$ (~17) | 13.2 | ~1 | [47] |
| Cu(100) and Cu(111) clusters derived from Cu-ade MOF | 0.1 M $KHCO_3$ solution | -1.4 (*vs.* RHE) | $C_2H_4$ (45) $CH_4$ (14) | 8.5 | 8 | [48] |
| Cu nanocube | 0.1 M $KHCO_3$ solution | -1.05 (*vs.* RHE) | $CH_4$ (~56) $C_2H_4$ (~20) | -- | ~5 | [49] |
| **Cu(111)@Cu-THQ** | **0.1 M $KHCO_3$ solution** | **-1.4 (*vs.* RHE)** | **$C_2H_4$ (42) $CH_4$(31)** | 6 | **8.5** | **This work** |

Density functional theory (DFT) calculations demonstrated that the Cu(100) crystal plane is more conducive to the formation of $C_2H_4$ because CO* is more easily adsorbed on the Cu(100) crystal plane and the energy barrier of CO* dimerization to form C-C is lower.[15]

# Supplementary References


[1] D. Kim, C. S. Kley, Y. Li, P. Yang, *Proc. Natl. Acad. Sci. USA* **2017**, *114*, 10560-10565.
[2] C. S. Chen, A. D. Handoko, J. H. Wan, L. Ma, D. Ren, B. S. Yeo, *Catal. Sci. Technol.* **2015**, *5*, 161-168.
[3] A. Loiudice, P. Lobaccaro, E. A. Kamali, T. Thao, B. H. Huang, J. W. Ager, R. Buonsanti, *Angew. Chem. Int. Ed.* **2016**, *55*, 5789-5792.
[4] H.-J. Yang, H. Yang, Y.-H. Hong, P.-Y. Zhang, T. Wang, L.-N. Chen, F.-Y. Zhang, Q.-H. Wu, N. Tian, Z.-Y. Zhou, S.-G. Sun, *ChemSusChem* **2018**, *11*, 881-887.
[5] D. Gao, I. Zegkinoglou, N. J. Divins, F. Scholten, I. Sinev, P. Grosse, B. Roldan Cuenya, *ACS Nano* **2017**, *11*, 4825-4831.
[6] Y. Kwon, Y. Lum, E. L. Clark, J. W. Ager, A. T. Bell, *ChemElectroChem* **2016**, *3*, 1012-1019.
[7] M. Ma, K. Djanashvili, W. A. Smith, *Angew. Chem. Int. Ed.* **2016**, *55*, 6680-6684.
[8] Z. Han, R. Kortlever, H.-Y. Chen, J. C. Peters, T. Agapie, *ACS Cent. Sci.* **2017**, *3*, 853-859.
[9] D. Ren, B. S.-H. Ang, B. S. Yeo, *ACS Catal.* **2016**, *6*, 8239-8247.
[10] Y. Wang, Z. Chen, P. Han, Y. Du, Z. Gu, X. Xu, G. Zheng, *ACS Catal.* **2018**, *8*, 7113-7119.
[11] G. Shi, L. Yu, X. Ba, X. Zhang, J. Zhou, Y. Yu, *Dalton Trans.* **2017**, *46*, 10569-10577.
[12] S. T. Ahn, I. Abu-Baker, G. T. R. Palmore, *Catal. Today* **2017**, *288*, 24-29.
[13] J. Resasco, L. D. Chen, E. Clark, C. Tsai, C. Hahn, T. F. Jaramillo, K. Chan, A. T. Bell, *J. Am. Chem. Soc.* **2017**, *139*, 11277-11287.
[14] R. Reske, H. Mistry, F. Behafarid, B. Roldan Cuenya, P. Strasser, *J. Am. Chem. Soc.* **2014**, *136*, 6978-6986.
[15] A. S. Varela, W. Ju, T. Reier, P. Strasser, *ACS Catal.* **2016**, *6*, 2136-2144.
[16] D. Ren, Y. Deng, A. D. Handoko, C. S. Chen, S. Malkhandi, B. S. Yeo, *ACS Catal.* **2015**, *5*, 2814-2821.
[17] X. Wang, A. S. Varela, A. Bergmann, S. Kühl, P. Strasser, *ChemSusChem* **2017**, *10*, 4642-4649.
[18] X. Tan, C. Yu, C. Zhao, H. Huang, X. Yao, X. Han, W. Guo, S. Cui, H. Huang, J. Qiu, *ACS Appl. Mater. Interfaces* **2019**, *11*, 9904-9910.
[19] Z. Weng, J. Jiang, Y. Wu, Z. Wu, X. Guo, K. L. Materna, W. Liu, V. S. Batista, G. W. Brudvig, H. Wang, *J. Am. Chem. Soc.* **2016**, *138*, 8076-8079.
[20] F. Yang, A. Chen, P. L. Deng, Y. Zhou, Z. Shahid, H. Liu, B. Y. Xia, *Chem. Sci.* **2019**, *10*, 7975-7981.
[21] P. Grosse, D. Gao, F. Scholten, I. Sinev, H. Mistry, B. Roldan Cuenya, *Angew. Chem. Int. Ed.* **2018**, *57*, 6192-6197.
[22] R. B. Sandberg, J. H. Montoya, K. Chan, J. K. Nørskov, *Surf. Sci.* **2016**, *654*, 56-62.